Journal Pre-proof

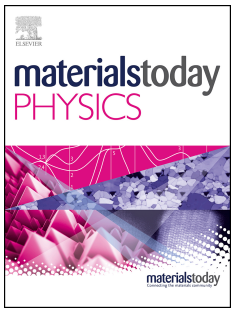

Point defect engineering and machinability in n-type Mg_3Sb_2-based materials

Juan Li, Shuai Zhang, Fei Jia, Shuqi Zheng, Xiaolei Shi, Daqiang Jiang, Siyu Wang, Guiwu Lu, Liming Wu, Zhi-Gang Chen

PII: S2542-5293(20)30093-6

DOI: https://doi.org/10.1016/j.mtphys.2020.100269

Reference: MTPHYS 100269

To appear in: *Materials Today Physics*

Received Date: 2 August 2020

Revised Date: 22 August 2020

Accepted Date: 23 August 2020

Please cite this article as: J. Li, S. Zhang, F. Jia, S. Zheng, X. Shi, D. Jiang, S. Wang, G. Lu, L. Wu, Z.-G. Chen, Point defect engineering and machinability in n-type Mg_3Sb_2-based materials, *Materials Today Physics*, https://doi.org/10.1016/j.mtphys.2020.100269.

Graphical Abstract

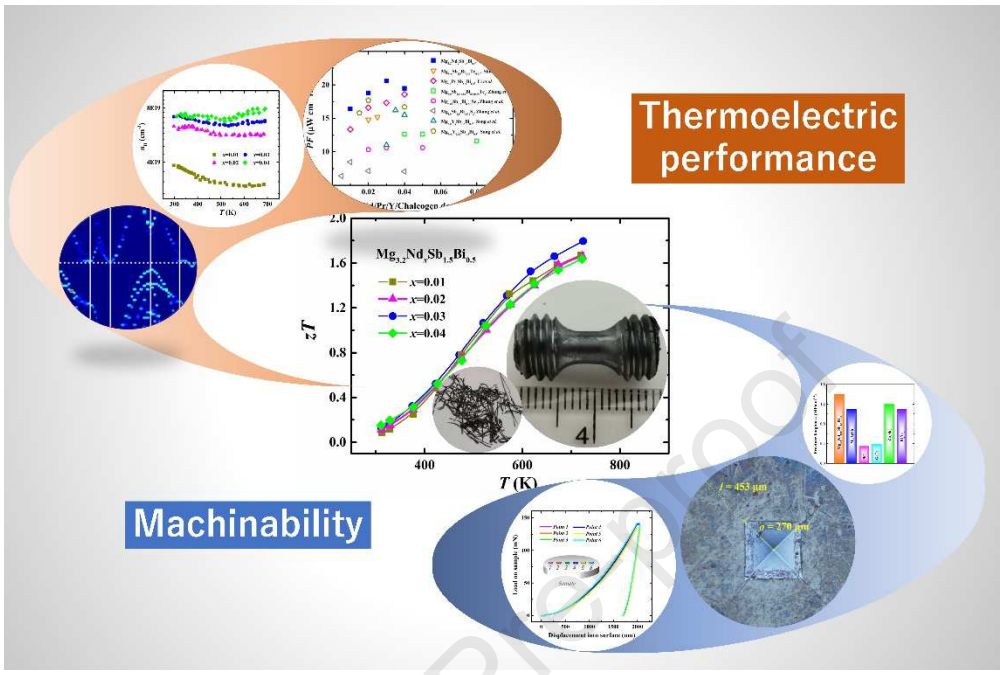

Point defect engineering and machinability in n-type Mg_3Sb_2-based materials

Juan Li[a,§], Shuai Zhang[a,§], Fei Jia[b], Shuqi Zheng[a,*], Xiaolei Shi[c], Daqiang Jiang[a], Siyu Wang[a], Guiwu Lu[a], Liming Wu[b], Zhi-Gang Chen[c,**]

[a] *State Key Laboratory of Heavy Oil Processing, College of New Energy and Materials, China University of Petroleum, Beijing 102249, People's Republic of China*

[b] *Beijing Key Laboratory of Energy Conversion and Storage Materials, College of Chemistry, Beijing Normal University, Beijing 100875, People's Republic of China*

[c] *Centre for Future Materials, University of Southern Queensland, Springfield Central, Queensland 4300, Australia*

[§]These authors contributed equally to this work.

Corresponding authors: [*]E-mail: zhengsq09@163.com (S. Zheng),

[**]E-mail: zhigang.chen@usq.edu.au; zhigang.chen@uq.edu.au (Z.-G. Chen).

Keywords: Mg_3Sb_2, machinability, defect engineering, thermoelectrics

Abstract

Approaching practical thermoelectric devices require high-performance and machinable thermoelectric materials. However, the currently available materials are usually brittle. In this work, Nd-doped Mg_3Sb_2-based compounds exhibit not only excellent thermoelectric performance but also superior machinability. $Mg_{3.2}Nd_{0.03}Sb_{1.5}Bi_{0.5}$ exhibits a high power factor of 20.6 μW cm^{-1} K^{-2} at 725 K and a peak zT of 1.8, which mainly originates from the increased n of ~8 × 10^{19} cm^{-3} by Nd/Mg substitutional defects. Defect calculations predict that other rare earth elements (Sm, Gd, Tb, Dy and Ho) have the same effect as Nd on Mg_3Sb_2 and the predicted highest achievable electron concentrations at 700 K are ~10^{20} cm^{-3}. The measured hardness, Young's modulus and fracture toughness of $Mg_{3.2}Nd_{0.03}Sb_{1.5}Bi_{0.5}$ are 1.1 GPa, 49.8 GPa and 1.4 MPa $m^{1/2}$, respectively. In addition, the sample can be easily machined into the dog-bone shape with external thread at both ends, indicating the excellent machinability of Mg_3Sb_2-based materials. This work suggests a bright future of Mg_3Sb_2-based thermoelectric materials for practical applications and device fabrication.

1. Introduction

Thermoelectric (TE) technology, enabling the direct conversion of waste heat into electricity based on Seebeck effect, has drawn increasing attention as a promising solution to energy crisis and environmental challenge [1-4]. The conversion efficiency is mainly governed by the Carnot efficiency and TE material's performance. Therefore, the key to the widespread use of this promising technology is to improve its dimensionless figure of merit (*zT*), $zT = S^2\sigma T / \kappa$, where S, σ, T and κ are the Seebeck coefficient, electrical conductivity, absolute temperature, and thermal conductivity, respectively [5-9]. The challenge of achieving higher *zT* lies in the fact that the TE parameters S, σ and κ are strongly coupled with each other. So far, strategies for improving *zT* are categorized into two approaches: maximizing the power factor ($PF = S^2\sigma$), such as, through band structure engineering or manipulation of carrier scattering mechanism, and reducing κ, for instance, via phonon scattering strengthening [10-13].

Recently, the n-type Te-doped $Mg_{3.2}Sb_{1.5}Bi_{0.5}$ with a prominent *zT* of 1.51 at 716 K was firstly reported by Tamaki *et al.* [14] and similar results have also been reported by other groups [15-18]. The role of Te substitution at Sb site was to increase the electron concentration to improve *PF* and the effect of Bi/Sb substitution was to reduce the lattice thermal conductivity (κ_L) [19-20]. The strategy based on defect engineering can be used for optimizing the carrer concentration (*n*), modulating the electronic band structure and reducing κ_L to to improve the thermoelectric performance of n-type Mg_3Sb_2-based materials [21-24]. Recently, both experimental

and theoretical investigations indicate that compared to Sb substitution with divalent anions (S, Se and Te) [18,25,26], Mg substitution with trivalent cations (La, Y and Pr) are more effective to achieve high *n* and thermoelectric properties [27-31]. This shows that investigating the doping behaviors of n-type dopants substitution at Mg sites is more important to the manipulation of the thermoelectric properties in Mg_3Sb_2-based materials. Therefore, this work is motivated to focus on realizing high thermoelectric performance through the controlling of point defects.

Besides the TE performance of materials, machinability and mechanical properties are also important to the large-scale application of their devices [32-37]. Poor machinability increases the difficulty of machining and thus lowers the yield. Recently, Qing Zhu *et al.* [38] reported that the Mg_3Sb_2-based TE device possessed a high conversion efficiency of 10.6% and had a good potential for mid-temperature heat conversion. Due to the brittle nature of most high-performance TE materials, it is an urgent issue to investigate the machinability and mechanical properties of Mg_3Sb_2-based materials to make sure the manufacturing and long-term reliability of TE devices.

In this work, using combined theoretical prediction and experimental validation, we report a new high-performance n-type thermoelectric material, $Mg_{3.2}Nd_xSb_{1.5}Bi_{0.5}$, that exhibits a high *PF* of 20.6 μW cm^{-1} K^{-2} and a peak *zT* of 1.8 at 725 K. Such an exceptionally high TE performance mainly originates from the increased *n* of ~8 × 10^{19} cm^{-3} by Nd/Mg substitutional defects. Using first-principles defect calculations, we predict that in addition to Nd, other rare earth elements (Sm, Gd, Tb, Dy and Ho)

are also effective n-type dopants in Mg_3Sb_2. The predicted highest achievable electron concentrations of these elements substitution on Mg sites at 700 K exceed 10^{20} cm^{-3}. Additionally, we find that the high-performance $Mg_{3.2}Nd_{0.03}Sb_{1.5}Bi_{0.5}$ sample displays extraordinary machinability. The cylindrical sample can be easily machined into the dog-bone shape with winding wires obtained during the lathing, and this phenomenon has also been observed in ductile inorganic α-Ag_2S semiconductor [39]. These results suggest that n-type Mg_3Sb_2-based materials have not only extraordinary thermoelectric performance but also superior machinability for practical applications and device fabrication.

2. Results and Discussion

Room-temperature X-ray diffraction (XRD) patterns of the sintered $Mg_{3.2}Nd_xSb_{1.5}Bi_{0.5}$ (x = 0.01, 0.02, 0.03 and 0.04) pellets are shown in Fig. S1. All the peaks can be indexed as the trigonal structure of α-Mg_3Sb_2 with a space group of $P\bar{3}m1$ (Standard Identification Card, JCPDS 65-9363) and there are no detectable impurities of other phases. From the enlarged XRD pattern, a slight left-shift can be observed, which suggests a lattice expansion in the samples because of the substitution of Mg with Nd. Both lattice parameters a and c show a nearly linear increasing trend with increasing the Nd content, which is attributed to the larger ionic radius for Nd^{3+} than Mg^{2+}.

The relative density of all the sintered samples are over 96% (Table S1). Fig. S2a-h shows the typical microstructure morphologies of the sintered samples, here we use $Mg_{3.2}Nd_{0.03}Sb_{1.5}Bi_{0.5}$ as an example. Fig. S2a is a typical transmission electron

microscopy (TEM) image of the specimen prepared by first manually polished to below 20 μm and then thinned using ion beam thinner (see Fig. S3), and shows a grain size of <1 μm. The high-resolution TEM (HRTEM) image clearly displays the lattice fringes with a lattice spacing of 0.33 nm, which corresponds to the (101) crystallographic plane of Mg_3Sb_2. The typical scanning electron microscopy (SEM) image of the freshly fractured surface confirms the dense sample with no obvious cracks or holes, consistent with the density measurement. The energy dispersive X-ray spectroscopy (EDS) mapping clearly shows that the elements (Mg, Nd, Sb and Bi) are present and distributed almost uniformly throughout the sample.

The dimensionless *zT* as a function of temperature for $Mg_{3.2}Nd_xSb_{1.5}Bi_{0.5}$ are shown in Fig. 1a and Fig. S4. Among all the sintered $Mg_{3.2}Nd_xSb_{1.5}Bi_{0.5}$, $Mg_{3.2}Nd_{0.03}Sb_{1.5}Bi_{0.5}$ exhibits the best peak *zT* of 1.80 at 725 K. *zT* values have good reproducibility (Fig. S5). In comparison to other n-type single-doped $Mg_{3+x}Sb_{1.5}Bi_{0.5}$ samples [14,18,25,26,28,29,31], our results display a higher *zT* at higher temperature as well as comparably good performance at lower temperature (Fig. 1a). Such an extraordinary n-type thermoelectric performance of n-type Mg_3Sb_2-based materials mainly originates from the enhancement of *PF* as shown in Fig. 1b. In comparison with the reported values [17,18,25,26,29,31], a significantly improved *PF* is realized in $Mg_{3.2}Nd_xSb_{1.5}Bi_{0.5}$ samples. Among the n-type samples, $Mg_{3.2}Nd_{0.03}Sb_{1.5}Bi_{0.5}$ exhibits the highest *PF* of 20.6 μW cm^{-1} K^{-2}, 94% higher than the value of 10.6 μW cm^{-1} K^{-2} for S-doped sample with the same doping content. This clearly indicates that the substitutional defect Nd/Mg makes a significant contribution to the high

thermoelectric performance of n-type $Mg_{3.2}Nd_xSb_{1.5}Bi_{0.5}$ samples.

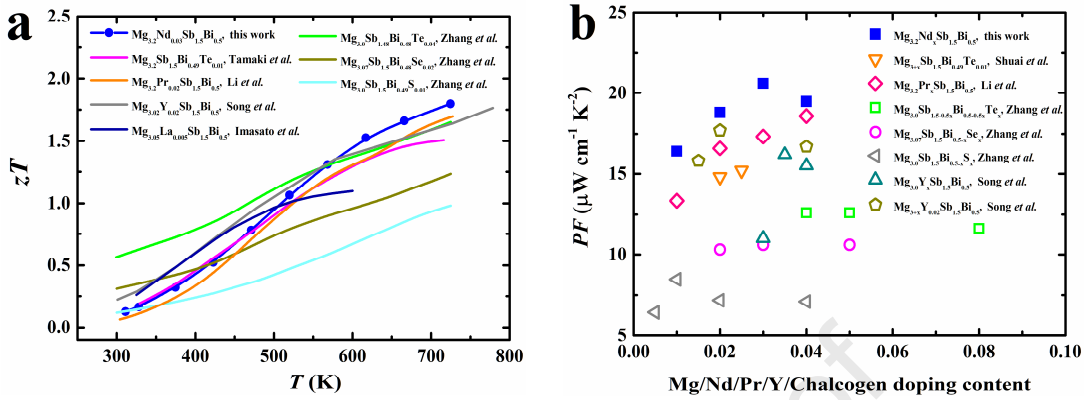

Fig. 1. (a) *zT* comparison of n-type $Mg_{3.2}Nd_{0.03}Sb_{1.5}Bi_{0.5}$ and other n-type Mg_3Sb_2-based thermoelectric materials [14,18,25,26,28,29,31]. (b) Mg/Nd/Pr/Y/Chalcogen doping content dependence of power factor of Mg_3Sb_2-based compounds at 725 K [17,18,25,26,29,31]. The blue squares are Nd doped samples from this work.

Fig. 2a shows the temperature-dependent Hall carrier concentration of $Mg_{3.2}Nd_xSb_{1.5}Bi_{0.5}$. The *n* increases with the increase of Nd doping amount, implying that Nd is an effective electron donor. The successful Nd/Mg substitution effectively increases the *n* as high as ~8×10^{19} cm^{-3}, consistent with the predicted maximal value of 7.9×10^{19} cm^{-3}. The electronic transport properties of the sintered $Mg_{3.2}Nd_xSb_{1.5}Bi_{0.5}$ pellets are shown in Fig. S6 and Fig. S7. The ρ and $|S|$ of $Mg_{3.2}Nd_xSb_{1.5}Bi_{0.5}$ (x = 0.02, 0.03 and 0.04) are much smaller than that of $Mg_{3.2}Nd_{0.01}Sb_{1.5}Bi_{0.5}$, which should be attributed to the much higher *n* of $Mg_{3.2}Nd_xSb_{1.5}Bi_{0.5}$ (x = 0.02, 0.03 and 0.04) than that of $Mg_{3.2}Nd_{0.01}Sb_{1.5}Bi_{0.5}$. The μ (Fig. S8) follows the relations $\mu \propto T^p$ ($1.9 \le p \le 3.9$) below 500 K and $\mu \propto T^{-1.3}$ above 500 K, suggesting that the electronic transports are dominated by ionized impurity scattering and acoustic phonon scattering, respectively.

To further illustrate the contribution of Nd/Mg substitutional defects to the *n*, defect formation energy calculations are conducted by density functional theory as shown in Fig. 2b. It clearly shows that the formation energy of the donor defect Nd_{Mg1} is lower than that of the acceptor defects V_{Mg1} and V_{Mg2}. As a result, the Fermi level (E_F) is pinned inside the conduction band. Therefore, we attribute the high *n* in $Mg_{3.2}Nd_xSb_{1.5}Bi_{0.5}$ samples to the introduction of the Nd/Mg substitutional defects. Compared to chalcogen substitution on Sb sites, rare earth elements (Nd, La, Y and Pr) substitution at Mg sites can introduce a higher electron concentration (Fig. 2c), which suggests that n-type doping at Mg sites possesses a higher doping efficiency for improving the thermoelectric performance. It can be concluded that n-type doping at Mg sites is more effective in increasing the electron concentration to make a good thermoelectric performance.

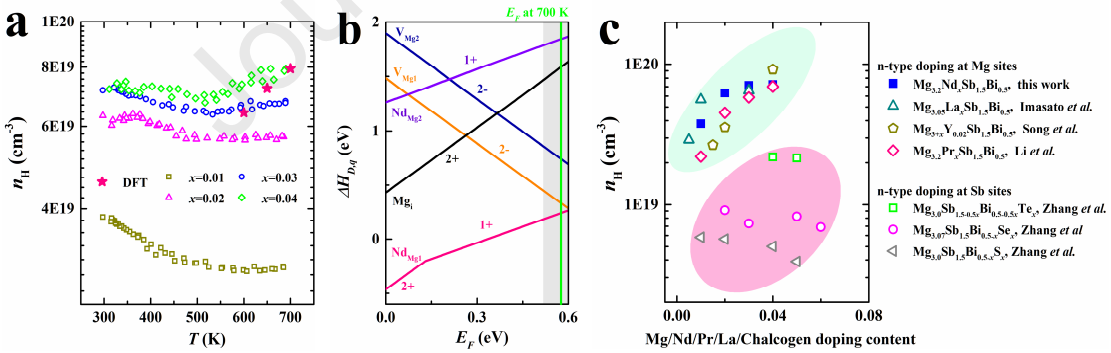

Fig. 2. (a) Temperature dependence of Hall carrier concentration of n-type $Mg_{3.2}Nd_xSb_{1.5}Bi_{0.5}$ (x = 0.01, 0.02, 0.03 and 0.04) samples. The pink stars are the predicted maximal achievable carrier concentration of n-type Nd-doped Mg_3Sb_2 under Mg-rich condition using first-principles defect calculations with density functional theory (DFT). (b) Defect formation energies of charged point defects as a function of Fermi level in Mg_3Sb_2 for n-type doping with Nd under Mg-rich condition. The shade region represents the conduction band. The green vertical line represents the Fermi level at 700 K. (c) Mg/Nd/Pr/La/Chalcogen doping content dependence of carrier concentration of

Mg_3Sb_2-based compounds at 300 K [18,25,26,28,29,31]. The blue squares are Nd doped samples from this work.

In addition to Nd, the doping behaviors of other rare earth elements (Sm, Gd, Tb, Dy and Ho) in Mg_3Sb_2 are also calculated as shown in Fig. 3. Defect energy calculations (Fig. 3a-e) show that the donor defects Sm_{Mg1}, Gd_{Mg1}, Tb_{Mg1}, Dy_{Mg1} and Ho_{Mg1} comparable in energy to the donor defect Nd_{Mg1} have much lower formation energy than the acceptor defects V_{Mg1} and V_{Mg2}, suggesting that Sm, Gd, Tb, Dy and Ho are also effective n-type dopants in Mg_3Sb_2. These substitutional defects can efficiently introduce a high concentration of electrons into the system. The predicted maximal free carrier concentrations of Sm-, Gd-, Tb-, Dy- and Ho-doped Mg_3Sb_2 (Fig. 3f) are in the range of 1×10^{20} – 1.3×10^{20} cm^{-3}. These results demonstrate that the high doping efficiencies for Sm, Gd, Tb, Dy and Ho are expected to achieve good thermoelectric properties of Mg_3Sb_2-based materials, similar to the case of Nd.

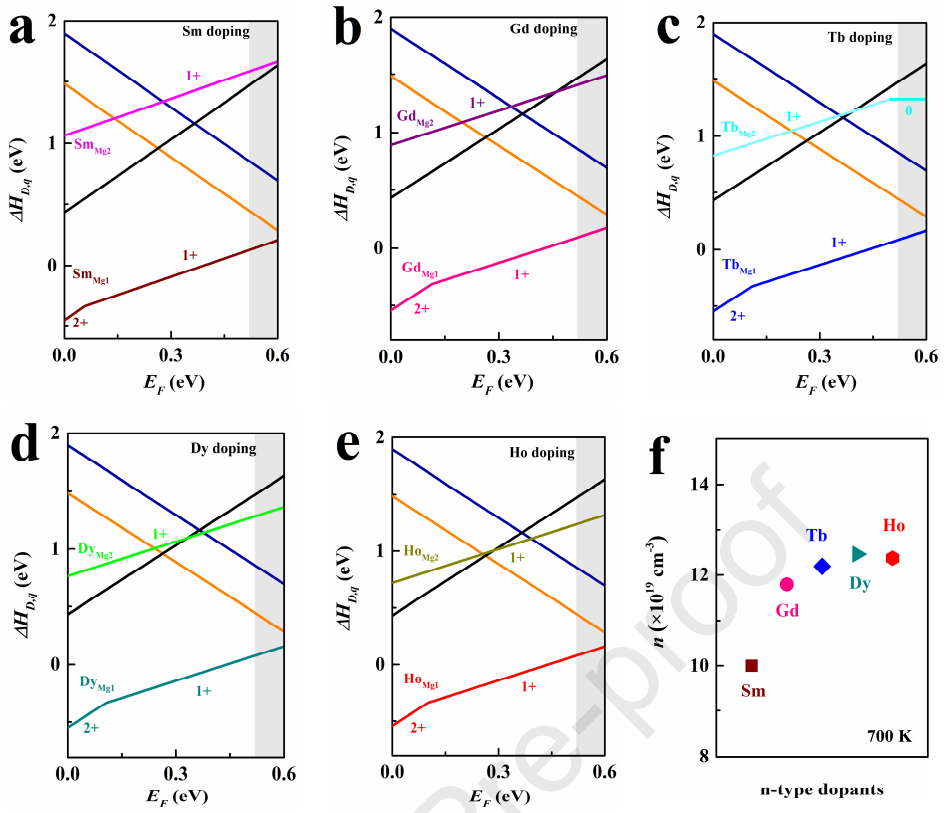

Fig. 3. Defect energies of n-type doping of Mg_3Sb_2 by cation substitution under Mg-rich condition. Doping with (a) Sm, (b) Gd, (c) Tb, (d) Dy and (e) Ho. (f) The maximal free carrier concentrations of n-type Sm-, Gd-, Tb-, Dy- and Ho-doped Mg_3Sb_2 under Mg-rich condition.

To reveal the substituting effect of Nd on the conduction band structure, the effective band structures of Mg_3Sb_2 with different Nd content are calculated and shown in Fig. 4. With increasing the Nd doping content, the M-band minimum shifts downward and approaches to the CB_1-band minimum, which may increase the contribution of the band minimum M to n-type carrier transports. In addition, the achieved high *n* with Nd doping (see Fig. 2a), which can place the Fermi level deep within the conduction band, is also helpful to increase the involvement of the M-band minimum to n-type carrier transports. In $Mg_{2.917}Nd_{0.083}Sb_{1.5}Bi_{0.5}$, the energy difference ($\Delta E_{\text{M-CB}_1}$) between the conduction band minima at the CB_1 point and M point

approaches to nearly zero, giving rise to a total valley degeneracy (N_v) up to 11. Therefore, Nd doping at Mg site is an effective way to enable the conduction band minimum M to contribute to the electronic transports. As Table S2 shows, the density of states effective mass (m_d^*) increases with the increase of Nd doping amount, which indicates that Nd doping is beneficial to *S* because *S* is proportional to m_d^* [18]. Besides Nd doping, Sm, Gd, Tb, Dy and Ho doping have similar effects on the conduction band structures of Mg_3Sb_2 (Fig. S9). In a conclusion, adopting rare earth elements doping in Mg_3Sb_2 can not only optimize the *n* but also increase the contribution of the band minimum M to n-type carrier transports. The collaborative optimization of *n* and $\Delta E_{M\text{-}CB_1}$ can be expected to be realized by tuning the suitable n-type dopants substitution on Mg sites.

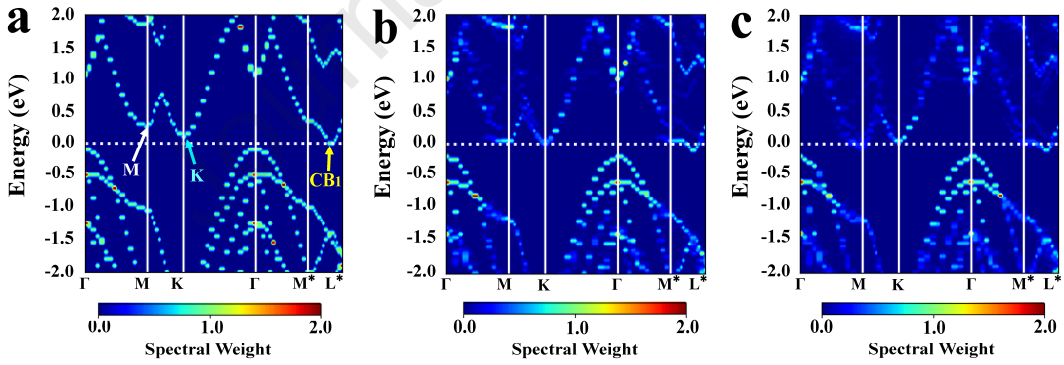

Fig. 4. The effective band structures of (a) pure Mg_3Sb_2, (b) $Mg_{2.944}Nd_{0.056}Sb_2$ and (c) $Mg_{2.917}Nd_{0.083}Sb_2$.

The temperature-dependent thermal transport properties of the sintered $Mg_{3.2}Nd_xSb_{1.5}Bi_{0.5}$ (x = 0.01, 0.02, 0.03 and 0.04) pellets are plotted in Fig. 5. The κ is the sum of electronic thermal conductivity (κ_e) and κ_L. With increasing the Nd content, κ exhibits a increasing trend, especially in the range of high temperature.

Using the Wiedemann–Franz relation [42], κ_e can be obtained by the relation $\kappa_e = LT/\rho$, where the Lorenz number (L) is calculated based on a single parabolic band (SPB) model with acoustic phonon scattering [43]. It is clear seen that the increasing κ is the result of the increasing fraction of κ_e. The obtained κ_L of all the samples by substracting κ_e from κ is shown in Fig. 5d. The low κ_L (0.48 W m^{-1} K^{-1}) of $Mg_{3.2}Nd_{0.03}Sb_{1.5}Bi_{0.5}$ at 725 K is in consistent with the Cahill's minimum κ_L of $Mg_3Sb_{1.5}Bi_{0.5}$ (0.49 W m^{-1} K^{-1}) [29].

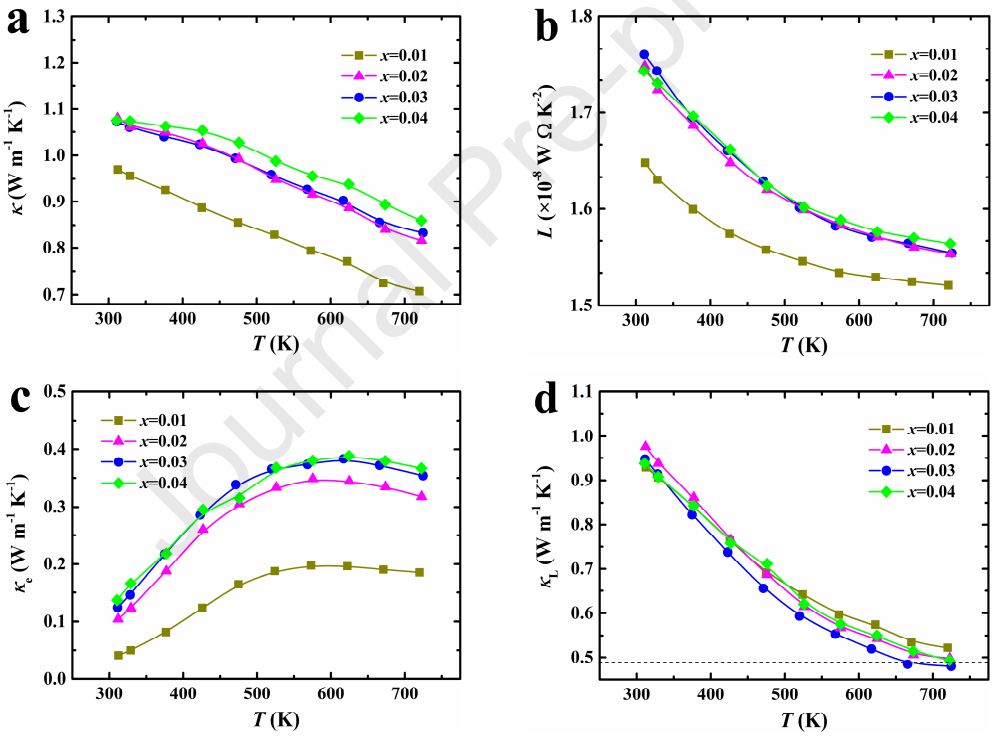

Fig. 5. Temperature dependence of (a) total thermal conductivity, (b) Lorenz number, (c) electronic thermal conductivity and (d) lattice thermal conductivity of n-type $Mg_{3.2}Nd_xSb_{1.5}Bi_{0.5}$ samples. In (d), the black short dash line represents the previously reported Cahill's minimum lattice thermal conductivity of $Mg_3Sb_{1.5}Bi_{0.5}$ [29].

Elastic constants, hardness and fracture toughness are crucial parameters for characterizing the mechanical properties. The measured Vickers hardness for

$Mg_{3.2}Nd_{0.03}Sb_{1.5}Bi_{0.5}$ is 1.1 GPa by indentation-crack measurements (Fig. 6a). The average Young's modulus is 49.8 GPa obtained from the nano-indentation experiments (Fig. 6b), comparable with the calculated value (46.4 GPa) for $Mg_3Sb_{1.5}Bi_{0.5}$ (Table S3). Based on Vickers indentation-crack technique, the fracture toughness of $Mg_{3.2}Nd_{0.03}Sb_{1.5}Bi_{0.5}$ is calculated to be 1.4 MPa $m^{1/2}$, higher than that of other state-of-art TE materials, as comparison in Fig. 6c [35,44-46]. The good toughness behavior of Mg_3Sb_2-based materials indicates a combination of high strength and ductility.

Based on the schematic diagram of Fig. 6d, the cylindrical $Mg_{3.2}Nd_{0.03}Sb_{1.5}Bi_{0.5}$ sample can be easily machined to the dog-bone shape with external thread at both ends (Fig. 6e), which demonstrates that Mg_3Sb_2-based materials have the potential to be processed into various shapes. The wires obtained during the lathing are very thin and winding (Fig. 6f). The ductile inorganic semiconductor α-Ag_2S also has the winding wires during the lathing [39]. The similar behavior of Mg_3Sb_2 and α-Ag_2S indicates the relatively good ductility of Mg_3Sb_2 in comparison with other high-performance TE materials. The good machinability and mechanical properties of Mg_3Sb_2-based materials can be further verfied in the TEM specimen preparation as shown in Fig. S3.

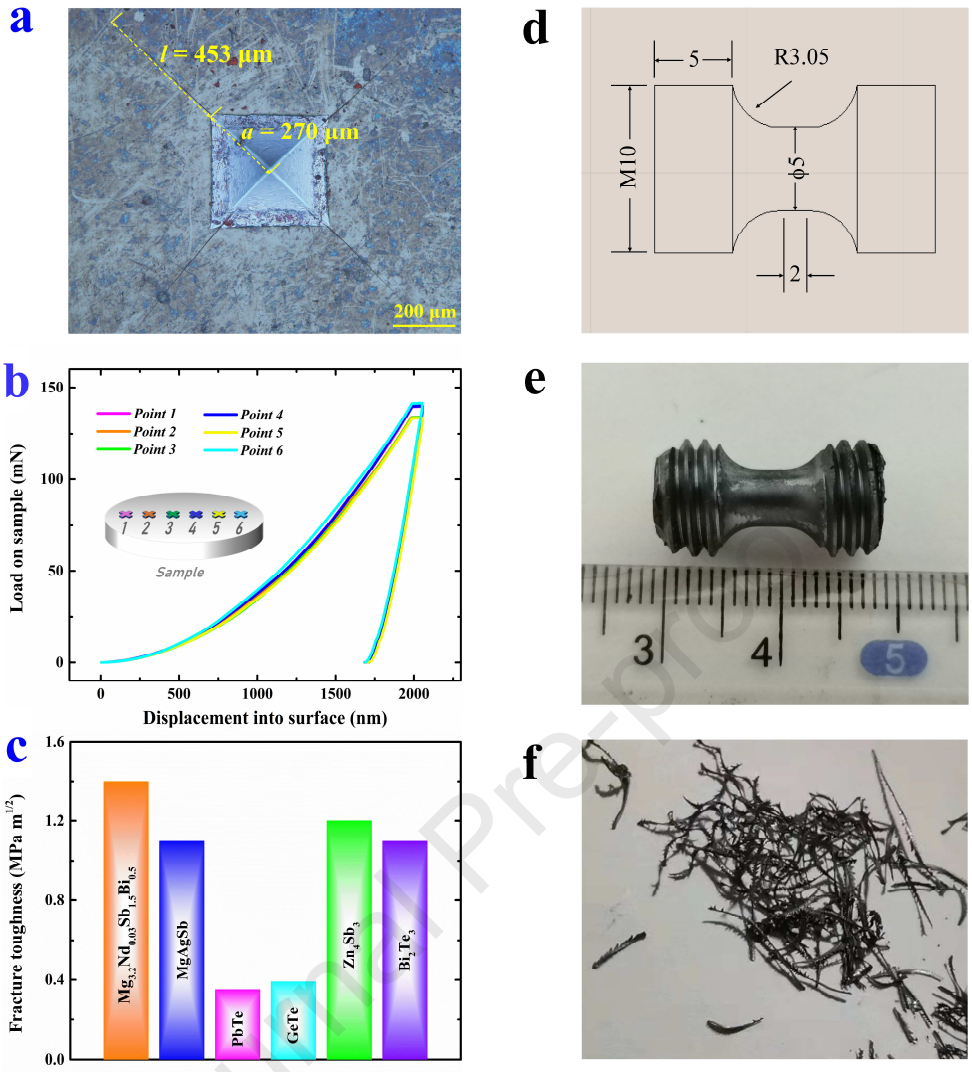

Fig. 6. (a) The optical microscopy image of Vickers indentation of $Mg_{3.2}Nd_{0.03}Sb_{1.5}Bi_{0.5}$ sample with marked indentation crack length *l* and the half-diagonal of indentation *a*. (b) The load-displacement nano-indentation curve of different positions (point 1, point 2, point 3, etc) on $Mg_{3.2}Nd_{0.03}Sb_{1.5}Bi_{0.5}$ sample surface. (c) The calculated fracture toughness of $Mg_{3.2}Nd_{0.03}Sb_{1.5}Bi_{0.5}$ and the comparison with other high-performance thermoelectric materials [35,44-46]. (d) Schematic diagram (in mm) of the dog-bone-shaped specimen. (e) Image of n-type $Mg_{3.2}Nd_{0.03}Sb_{1.5}Bi_{0.5}$ sample after the lathing. (f) The obtained thin and winding wires during the lathing.

3. Conclusions

In this work, we investigated the thermoelectric performance and machinability

of n-type Mg_3Sb_2-based materials. $Mg_{3.2}Nd_{0.03}Sb_{1.5}Bi_{0.5}$ exhibits a high *PF* of 20.6 μW cm^{-1} K^{-2} at 725 K and a peak *zT* of 1.8. Combined theoretical and experimental investigations, it is found that the exceptional performance mainly originates from the largely increased carrier concentration by Nd/Mg substitution defects. First-princples defect calculations demonstrate that other rare earth elements (Sm, Gd, Tb, Dy and Ho) are also effective n-type dopants in Mg_3Sb_2 and the predicted highest achievable electron concentrations at 700 K exceed 10^{20} cm^{-3}. In addition, we find that Mg_3Sb_2-based materials possess better machinability and mechanical properties in comprison with other high-performance TE materials, and have the potential to be processed into various shapes for practical applications. In conclusion, the superior machinability coupled with high thermoelectric performance indicate that n-type Mg_3Sb_2-based material is a good candidate for mid temperature power generation application.

4. Methods

Sample Synthesis: Samples with nominal compositions $Mg_{3.2}Nd_xSb_{1.5}Bi_{0.5}$ (x = 0.01, 0.02, 0.03 and 0.04) were prepared by planetary ball milling (BM40, Beijing Grinder Instrument Co., Ltd.) combined with spark plasma sintering (SPS, SPS-211LX, Fuji Electronic Industrial Co., Ltd.). High-purity powders of magnesium (Mg, 99.5%, Aladdin Co., Ltd.), antimony (Sb, 99.5%, Aladdin Co., Ltd.), bismuth (Bi, 99.9%, Aladdin Co., Ltd.) and neodymium (Nd, 99.9%, Alfa Aesar) were weighed in an argon-filled glove box with an oxygen level below 0.5 ppm and then

loaded into a zirconia ball milling jar. The ball milling was performed with a rotational speed of 360 rpm for 4.5 hours. The black powder was loaded into a graphite die in a glove box and then sintered by SPS pressing in a vacuum at 650 □ for 5 min under a pressure of 50 MPa.

Structure Characterization: X-ray diffraction measurements were performed on the SPS-pressed pellets using Bruker D8 diffractometer equipped with Cu Kα (λ =1.5406 Å) radiation. Jade software was used to calculate the lattice parameters. The microstructure morphology was investigated by a scanning electron microscope (SEM, FEI Quanta 200F) and a transmission electron microscopy (TEM, FEI Tecnai G^2 F20).

Thermoelectric Transport Property Measurements: ρ and S were measured by ZEM-3 (Ulvac Riko, Inc.) under a helium atmosphere. Thermal conductivity $\kappa=dDc_p$ was calculated using the density (d) determined by the Archimedes method, specific heat (c_p) obtained from a study previously published by Agne *et al.* [47] and thermal diffusivity (D) measured by a laser flash method with a Netzsch LFA-457 instrument under a nitrogen atmosphere. The Hall coefficient (R_H) was measured using the van der Pauw technique under a reversible magnetic field of 1.5 T. Hall carrier concentration (n_H) and mobility (μ_H) were obtained by the relations $n_H = 1/eR_H$ and $\mu_H = R_H/\rho$.

Mechanical Property Measurements: The cylinder sample with dimensions of $\phi 10\times 18\,\mathrm{mm}^3$ was prepared for the lathe. A polished disc with a thickness of about 2 mm was used to measure the Vickers hardness by digital metallic Vickers hardness

tester (SCTMC) with a load of 196.1 N for 15 s. The Vickers indentation was observed and analyzed by DSX510 Olympus microscope**.** Nanoindentation experiment was performed on an Agilent Nano indenter G200 and the elastic modulus was determined from the measured load penetration depth curves. The fracture toughness (K_{IC}) measurement was based on Vickers indentation-crack technique according to the method proposed by Niihara *et al.* [48],

$$K_{IC} = 0.0089\left(\frac{E}{HV}\right)^{2/5} \times \frac{P}{al^{1/2}}, \quad 0.25 \le \frac{l}{a} \le 2.5 \tag{1}$$

where E is the Young's modulus (GPa), HV is the Vickers hardness (GPa), P is the load applied in the hardness test (N), a is the half-diagonal of Vickers indentation (m), and l is the surface crack length (m).

Density Functional Theory (DFT) Calculations: DFT calculations were carried out by the projector augmented wave (PAW) method as implemented in the Vienna ab initio simulation package (VASP) [49-52]. The optimized structure parameters of Mg_3Sb_2 from our previous work [41] were adopted. The first-principles defect calculations were performed on a 2 × 2 × 2 supercell of the primitive cell by HSE06 functional [53]. The calculation details are provided in the Supporting Information. The electronic band structures of $Mg_{2.944}A_{0.056}Sb_2$ (A = Nd, Sm, Gd, Tb, Dy, Ho and La) and $Mg_{2.917}Nd_{0.083}Sb_2$ were calculated by PBE functional [54] respectively in 3 × 3 × 2 supercell and 3 × 2 × 2 supercell of the primitive cell. BandUP code [52,55] was applied to unfold the band structure of the supercell into the primitive cell. A plane-wave cutoff energy of 400 eV and an energy convergence criterion of 10^{-4} eV were employed. A 2 × 2 × 2 Γ-centered k mesh was adopted.

Conflicts of interest

The authors declare no competing financial interest.

Acknowledgements

This work was financially supported by the Natural Science Foundation of China (No. 51871240) and Australian Research Council. The calculations were carried out on the National Supercomputing Center in Shenzhen (Shenzhen Cloud Computing Center).

References

[1] Z. G. Chen, X. Shi, L. D. Zhao, J. Zou, High-performance SnSe thermoelectric materials: Progress and future challenge, Prog. Mater. Sci. 97 (2018) 283–346.

[2] W. He, D. Wang, H. Wu, Y. Xiao, Y. Zhang, D. He, Y. Feng, Y. Hao, J. Dong, R. Chetty, L. Hao, D. Chen, J. Qin, Q. Yang, X. Li, J. Song, Y. Zhu, W. Xu, C. Niu, X. Li, G. Wang, C. Liu, M. Ohta, S. J. Pennycook, J. He, J. Li, L. Zhao, High thermoelectric performance in low-cost $SnS_{0.91}Se_{0.09}$ crystals, Science 365 (2019) 1418–1424.

[3] L. Zhao, G. Tan, S. Hao, J. He, Y. Pei, H. Chi, H. Wang, S. Gong, H. Xu, V. P. Dravid, C. Uher, G. J. Snyder, C. Wolverton, M. G. Kanatzidis, Ultrahigh power factor and thermoelectric performance in hole-doped single-crystal SnSe, Science 351 (2016) 141–144.

[4] J. Shuai, J. Mao, S. Song, Q. Zhang, G. Chen, Z. Ren, Recent progress and future challenges on thermoelectric Zintl materials, Mater. Today Phys. 1 (2017) 74–95.

[5] Z. Liu, J. Mao, S. Peng, B. Zhou, W. Gao, J. Sui, Y. Pei, Z. Ren, Tellurium doped n-type Zintl $Zr_3Ni_3Sb_4$ thermoelectric materials: Balance between carrier-scattering mechanism and bipolar effect, Mater. Today Phys. 2 (2017) 54–61.

[6] J. Sun, J. Shuai, Z. Ren, D. J. Singh, Computational modelling of the thermoelectric properties of p-type Zintl compound $CaMg_2Bi_2$, Mater. Today Phys. 2 (2017) 40–45.

[7] T. Zhou, L. Wang, S. Zheng, M. Hong, T. Fang, P. Bai, S. Chang, W. Cui, X. Shi, H. Zhao, Z. G. Chen, Self-assembled 3D flower-like hierarchical Ti-doped Cu_3SbSe_4 microspheres with ultralow thermal conductivity and high zT, Nano Energy 49 (2018) 221–229.

[8] Y. Wang, L. Yang, X. L. Shi, X. Shi, L. Chen, M. S. Dargusch, J. Zou, Z. G. Chen, Flexible thermoelectric materials and generators: challenges and innovations, Adv. Mater. 31 (2019) 1807916.

[9] J. Xin, G. Li, G. Auffermann, H. Borrmann, W. Schnelle, J. Gooth, X. Zhao, T. Zhu, C. Felser, C. Fu, Growth and transport properties of Mg_3X_2 (X= Sb, Bi) single crystals, Mater. Today Phys. 7 (2018) 61–68.

[10] J. Mao, H. Zhu, Z. Ding, Z. Liu, G. A. Gamage, G. Chen, Z. Ren, High thermoelectric cooling performance of n-type Mg_3Bi_2-based materials, Science 365 (2019) 495–498.

[11] X. Chen, H. Wu, J. Cui, Y. Xiao, Y. Zhang, J. He, Y. Chen, J. Cao, W. Cai, S. J. Pennycook, Z. Liu, L. Zhao, J. Sui, Extraordinary thermoelectric performance in n-type manganese doped Mg_3Sb_2 Zintl: High band degeneracy, tuned carrier scattering mechanism and hierarchical microstructure, Nano Energy 52 (2018) 246–255.

[12] K. Imasato, S. D. Kang, G. J. Snyder, Exceptional thermoelectric performance in $Mg_3Sb_{0.6}Bi_{1.4}$ for low-grade waste heat recovery, Energy Environ. Sci. 12 (2019) 965–971.

[13] M. Hong, T. C. Chasapis, Z. G. Chen, L. Yang, M. G. Kanatzidis, G. J. Snyder, J. Zou, N-type $Bi_2Te_{3-x}Se_x$ nanoplates with enhanced thermoelectric efficiency driven by wide-frequency phonon scatterings and synergistic carrier scatterings, ACS Nano 10 (2016) 4719–4727.

[14] H. Tamaki, H. K. Sato, T. Kanno, Isotropic conduction network and defect chemistry in $Mg_{3+\delta}Sb_2$-based layered Zintl compounds with high thermoelectric performance, Adv. Mater. 28 (2016) 10182–10187.

[15] K. Imasato, S. D. Kang, S. Ohno, G. J. Snyder, Band engineering in Mg_3Sb_2 by alloying with Mg_3Bi_2 for enhanced thermoelectric performance, Mater. Horiz. 5 (2018) 59–64.

[16] S. Ohno, K. Imasato, S. Anand, H. Tamaki, S. D. Kang, P. Gorai, H. K. Sato, E. S. Toberer, T. Kanno, G. J. Snyder, Phase boundary mapping to obtain n-type Mg_3Sb_2-based thermoelectrics, Joule 2 (2017) 141–154.

[17] J. Shuai, B. Ge, J. Mao, S. Song, Y. Wang, Z. Ren, Significant role of Mg stoichiometry in

designing high thermoelectric performance for $Mg_3(Sb,Bi)_2$-based n-type Zintls, J. Am. Chem. Soc. 140 (2018) 1910–1915.

[18] J. Zhang, L. Song, S. H. Pedersen, H. Yin, L. T. Hung, B. B. Iversen, Discovery of high-performance low-cost n-type Mg_3Sb_2-based thermoelectric materials with multi-valley conduction bands, Nat. Commun. 8 (2017) 13901.

[19] J. Zhang, L. Song, B. B. Iversen, Insights into the design of thermoelectric Mg_3Sb_2 and its analogs by combining theory and experiment, npj Comput. Mater. 5 (2019) 76.

[20] J. Zhang, B. B. Iversen, Fermi surface complexity, effective mass, and conduction band alignment in n-type thermoelectric $Mg_3Sb_{2-x}Bi_x$ from first principles calculations, J. Appl. Phys. 126 (2019) 085104.

[21] J. Mao, Y Wu, S. Song, Q. Zhu, J. Shuai, Z. Liu, Y. Pei, Z. Ren, Defect engineering for realizing high thermoelectric performance in n-type Mg_3Sb_2-based materials, ACS Energy Lett. 2 (2017) 2245–2250.

[22] A. Banik, U. S. Shenoy, S. Anand, U. V. Waghmare, K. Biswas, Mg alloying in SnTe facilitates valence band convergence and optimizes thermoelectric properties, Chem. Mater. 27 (2015) 581–587.

[23] J. Li, W. Li, Z. Bu, X. Wang, B. Gao, F. Xiong, Y. Chen, Y. Pei, Thermoelectric transport properties of $Cd_xBi_yGe_{1-x-y}Te$ Alloys, ACS Appl. Mater. Inter. 10 (2018) 39904–39911.

[24] J. Shuai, J. Mao, S. Song, Q. Zhu, J. Sun, Y. Wang, R. He, J. Zhou, G. Chen, D. J. Singh, Z. Ren, Tuning the carrier scattering mechanism to effectively improve the thermoelectric properties, Energy Environ. Sci. 10 (2017) 799–807.

[25] J. Zhang, L. Song, K. A. Borup, M. R. V. Jørgensen, B. B. Iversen, New insight on tuning electrical transport properties via chalcogen doping in n-type Mg_3Sb_2-based thermoelectric materials, Adv. Energy Mater. 8 (2018) 1702776.

[26] J. Zhang, L. Song, A. Mamakhel, M. R. V. Joergensen, B. B. Iversen, High-performance low-cost n-type Se-doped Mg_3Sb_2-based Zintl compounds for thermoelectric application, Chem. Mater. 29 (2017) 5371–5383.

[27] P. Gorai, B. R. Ortiz, E. S. Toberer, V. Stevanović, Investigation of n-type doping strategies for Mg_3Sb_2, J. Mater. Chem. A 6 (2018) 13806–13815.

[28] K. Imasato, M. Wood, J. J. Kuo, G. J. Snyder, Improved stability and high thermoelectric

performance through cation site doping in n-type La-doped $Mg_3Sb_{1.5}Bi_{0.5}$, J. Mater. Chem. A 6 (2018) 19941–19946.

[29] J. Li, F. Jia, S. Zhang, S. Zheng, B. Wang, L. Chen, G. Lu, L. Wu, The manipulation of substitutional defects for realizing high thermoelectric performance in Mg_3Sb_2-based Zintl compounds, J. Mater. Chem. A 7 (2019) 19316–19323.

[30] J. Li, S. Zhang, S. Zheng, Z. Zhang, B. Wang, L. Chen, G. Lu, Defect chemistry for n-type doping of Mg_3Sb_2-based thermoelectric materials, J. Phys. Chem. C 123 (2019) 20781–20788.

[31] S. Song, J. Mao, M. Bordelon, R. He, Y. Wang, J. Shuai, J. Sun, X. Lei, Z. Ren, S. Chen, S. Wilson, K. Nielsch, Q. Zhang, Z. Ren, Joint effect of magnesium and yttrium on enhancing thermoelectric properties of n-type Zintl $Mg_{3+\delta}Y_{0.02}Sb_{1.5}Bi_{0.5}$, Mater. Today Phys. 8 (2019) 25–33.

[32] T. Wei, M. Jin, Y. Wang, H. Chen, Z. Gao, K. Zhao, P. Qiu, Z. Shan, J. Jiang, R. Li, L. Chen, J. He, X. Shi, Exceptional plasticity in the bulk single-crystalline van der Waals semiconductor InSe, Science 369 (2020) 542–545.

[33] Z. Zhou, J. Li, Y. Fan, Q. Zhang, X. Lu, S. Fan, K. Kikuchi, N. Nomura, A. Kawasaki, L. Wang, W. Jiang, Uniform dispersion of SiC in Yb-filled skutterudite nanocomposites with high thermoelectric and mechanical performance, Scripta Mater. 162 (2019) 166–171.

[34] K. Yin, X. Su, Y. Yan, H. Tang, M. G. Kanatzidis, C. Uher, X. Tang, Morphology modulation of SiC nano-additives for mechanical robust high thermoelectric performance $Mg_2Si_{1-x}Sn_x$/SiC nano-composites, Scripta Mater. 126 (2017) 1–5.

[35] G. M. Guttmann, Y. Gelbstein, Bringing Thermoelectricity into Reality, 2018, http://dx.doi.org/10.5772/intechopen.75476.

[36] Y. Zhu, P. Wu, J. Guo, Y. Zhou, X. Chong, Z. Ge, J. Feng, Achieving a fine balance in mechanical properties and thermoelectric performance in commercial Bi_2Te_3 materials, Ceram. Int. 46 (2020) 14994–15002.

[37] Y. Zheng, Q. Zhang, X. Su, H. Xie, S. Shu, T. Chen, G. Tan, Y. Yan, X. Tang, C. Uher, G. J. Snyder, Mechanically robust BiSbTe alloys with superior thermoelectric performance: a case study of stable hierarchical nanostructured thermoelectric materials, Adv. Energy Mater. 5 (2015) 1401391.

[38] Q. Zhu, S. Song, H. Zhu, Z. Ren, Realizing high conversion efficiency of Mg_3Sb_2–based thermoelectric materials, J. Power Sources 414 (2019) 393–400.

[39] X. Shi, H. Chen, F. Hao, R. Liu, T. Wang, P. Qiu, U. Burkhardt, Y. Grin, L. Chen, Room-temperature ductile inorganic semiconductor, Nat. Mater. 17 (2018) 421–426.

[40] J. Li, S. Zhang, B. Wang, S. Liu, L. Yue, G. Lu, S. Zheng, Designing high-performance n-type Mg_3Sb_2-based thermoelectric materials through forming solid solutions and biaxial strain, J. Mater. Chem. A 6 (2018) 20454–20462.

[41] J. Li, S. Zheng, T. Fang, L. Yue, S. Zhang, G. Lu, Computational prediction of a high ZT of n-type Mg_3Sb_2-based compounds with isotropic thermoelectric conduction performance, Phys. Chem. Chem. Phys. 20 (2018) 7686–7693.

[42] J. Li, Z. Chen, X. Zhang, H. Yu, Z. Wu, H. Xie, Y. Chen, Y. Pei, Simultaneous optimization of carrier concentration and alloy scattering for ultrahigh performance GeTe thermoelectrics, Adv. Sci. 4 (2017) 1700341.

[43] L. Zhao, S. Lo, J. He, H. Li, K. Biswas, J. Androulakis, C. Wu, T. P. Hogan, D. Chung, V. P. Dravid, M. G. Kanatzidis, High performance thermoelectrics from earth-abundant materials: enhanced figure of merit in PbS by second phase nanostructures, J. Am. Chem. Soc. 133 (2011) 20476–20487.

[44] Z. Liu, W. Gao, X. Meng, X. Li, J. Mao, Y. Wang, J. Shuai, W. Cai, Z. Ren, J. Sui, Mechanical properties of nanostructured thermoelectric materials α-MgAgSb, Scripta Mater. 127 (2017) 72–75.

[45] S. C. Ur, P. Nash, R. Schwarz, Mechanical and thermoelectric properties of Zn_4Sb_3 and Zn_4Sb_3+Zn directly synthesized using elemental powders, Met. Mater. Int. 11 (2005) 435.

[46] L. Zhao, B. Zhang, J. Li, M. Zhou, W. Liu, J. Liu, Thermoelectric and mechanical properties of nano-SiC-dispersed Bi_2Te_3 fabricated by mechanical alloying and spark plasma sintering, J. Alloys Compd. 455 (2008) 259–264.

[47] M. T. Agne, K. Imasato, S. Anand, K. Lee, S. K. Bux, A. Zevalkink, A. J. E. Rettie, D. Y. Chung, M. G. Kanatzidis, G. J. Snyder, Heat capacity of Mg_3Sb_2, Mg_3Bi_2, and their alloys at high temperature, Mater. Today Phys. 6 (2018) 83–88.

[48] K. Niihara, R. Morena, D. P. H. Hasselman, Evaluation of K_{Ic} of brittle solids by the indentation method with low crack-to-indent ratios, J. Mater. Sci. Lett. 1 (1982) 13–16.

[49] B. Hammer, L. B. Hansen, J. K. Nørskov, Improved adsorption energetics within density-functional theory using revised Perdew-Burke-Ernzerhof functionals, Phys. Rev. B: Condens. Matter Mater. Phys. 59 (1999) 7413–7421.

[50] P. E. Blöchl, Projector augmented-wave method, Phys. Rev. B: Condens. Matter Mater. Phys. 50 (1994) 17953.

[51] G. Kresse, J. Furthmuller, Efficiency of ab-initio total energy calculations for metals and semiconductors using a plane-wave basis set, Comput. Mater. Sci. 6 (1996) 15–50.

[52] P. V. C. Medeiros, S. Stafström, J. Björk, Effects of extrinsic and intrinsic perturbations on the electronic structure of graphene: Retaining an effective primitive cell band structure by band unfolding, Phys. Rev. B: Condens. Matter Mater. Phys. 89 (2014) 041407.

[53] J. Paier, M. Marsman, K. Hummer, G. Kresse, I. C. Gerber, J. G. Ángyán, Erratum: "Screened hybrid density functionals applied to solids" [J. Chem. Phys. 124, 154709 (2006)], J. Chem. Phys. 125 (2006) 249901.

[54] J. P. Perdew, K. Burke, M. Ernzerhof, Generalized gradient approximation made simple, Phys. Rev. Lett. 77 (1996) 3865–3868.

[55] P. V. C. Medeiros, S. S. Tsirkin, S. Stafström, J. Björk, Unfolding spinor wave functions and expectation values of general operators: Introducing the unfolding-density operator, Phys. Rev. B: Condens. Matter Mater. Phys. 91 (2015) 041116.

Highlights:

- Adopting n-type doping at Mg sites can increase carrier concentration and affect the M-band minimum.
- A high power factor of 20.6 μW cm^{-1} K^{-2} and figure of merit of 1.8 are reported in $Mg_{3.2}Nd_{0.03}Sb_{1.5}Bi_{0.5}$.
- Compared to other state-of-art TE materials, Mg_3Sb_2-based materials exhibit better machinability and mechanical properties.

Declaration of interests

☑ The authors declare that they have no known competing financial interests or personal relationships that could have appeared to influence the work reported in this paper.

☐The authors declare the following financial interests/personal relationships which may be considered as potential competing interests:

Author contributions

J. Li, S. Zhang and S. Zheng designed the experiments; J. Li, S. Zhang, F. Jia, S. Zheng and L. Wu performed the material synthesis and sample measurement; J. Li and S. Zhang performed the mechanical property measurement. J. Li, S. Wang and G. Lu performed the theoretical calculation. X. Shi, D. Jiang and Z.-G. Chen conducted the SEM and TEM characterization. Everyone was involved in writing the article.